Numerical and experimental analysis of a planar jet with heated co-flow at medium and low Prandtl-number values

Cascioli, E.; Buckingham, S.; Keijers, S.; Tichelen, K. Van; Kenjeres, Sasa

DOI
10.1016/j.nucengdes.2020.110570

Publication date
2020

Document Version
Proof

Published in
Nuclear Engineering and Design

Nuclear Engineering and Design xxx (xxxx) xxxx

Contents lists available at ScienceDirect

Nuclear Engineering and Design

journal homepage: www.elsevier.com/locate/nucengdes

Numerical and experimental analysis of a planar jet with heated co-flow at medium and low Prandtl-number values

E. Cascioli[a,b], S. Buckingham[c], S. Keijers[b], K. Van Tichelen[b], Sasa Kenjeres[a,*]

[a] TUD, Delft University of Technology, Faculty of Applied Sciences, Department of Chemical Engineering, Transport Phenomena Section and J. M. Burgerscentrum Research School for Fluid Mechanics, Van der Maasweg 9, 2629 HZ Delft, The Netherlands
[b] SCK·CEN, Belgian Nuclear Research Centre, Boeretang 200, 2400 Mol, Belgium
[c] VKI, von Karman Institute for Fluid Dynamics, Waterloosesteenweg 72, 1640 Sint-Genesius-Rode, Belgium

ARTICLE INFO

Keywords:
Planar jet
Forced convection
Low Prandtl number
Two-equation heat transfer model

ABSTRACT

In the present work, we combine experiments and numerical simulations of a planar jet with heated co-flow with medium (air) and low-Prandtl (He-Xe gas mixture) fluids. Jets are recognized as representative test cases to be investigated in large components of pool-type liquid metal-cooled nuclear systems, like the Multi-purpose hYbrid Research Reactor for High-tech Applications (MYRRHA), currently under design at SCK•CEN. The present planar jet configuration mimics a closed wind tunnel that is designed and operated at VKI to generate an experimental database for velocity and temperature fields of a turbulent forced-convection flow regime. The performed experiments combine the Particle Imaging Velocimetry (PIV) (in characteristic planes) and thermocouple (single point) measurements. In parallel with experiments, comprehensive numerical simulations have been performed within the RANS modeling framework. Next to the standard eddy-viscosity based two-equation $k-\varepsilon$ model, an extended variant based on the low-Reynolds elliptic relaxation concept (so-called $\zeta-f$ model) has been applied too. To investigate the low-Prandtl effects on the heat transfer, series of the turbulent heat transfer models have been applied, ranging from a conventional constant turbulent Prandtl number to a more elaborate $k_\theta-\varepsilon_\theta$ model. The combination of the low-Reynolds $\zeta-f$ and $k_\theta-\varepsilon_\theta$ models was explored for the first time in the content of nuclear engineering applications. The focus of the numerical studies is to address in details the effects of low-Prandtl fluid in the strongly forced convection flow (central planar cold jet) in presence of a strong shear (hot co-flow). We demonstrate the importance of the proper specification of the inlet boundary conditions in numerical simulations to mimic correctly experimentally observed asymmetrical distributions of the cross-wise profiles of stream-wise velocity, turbulent kinetic energy and temperature. Finally, the minor differences in results between the assumed constant turbulent Prandtl number and more advanced $k_\theta-\varepsilon_\theta$ model of the turbulent heat flux confirmed the overly dominant mechanisms of the strong convection and molecular diffusion in the present configuration.

1. Introduction

The Multi-purpose hYbrid Research Reactor for High-tech Applications (MYRRHA) is a flexible fast-spectrum research reactor under design at SCK•CEN. MYRRHA is a pool-type reactor cooled by the liquid metal Lead–Bismuth Eutectic (LBE) and contributes to the demonstration of transmutation of long-lived radioactive waste. It also represents a prototype of the next generation of the fast reactor technology cooled by liquid metals, Fernandez et al. (2017). The high safety standards require a good understanding of heat transfer phenomena in liquid metals. Experiments are necessary to understand the mass, momentum, and heat transfer physics and validate the engineering models used in Computational Fluid Dynamics (CFD) codes, supporting the design and safety analyses of such advanced nuclear systems, Van Tichelen et al. (2015). Industrial CFD analyses are commonly based on Reynolds Averaged Navier–Stokes (RANS) simulations, where the Reynolds analogy is the standard approach in representing the turbulent heat transfer. This implies modeling turbulent heat fluxes analogously to Reynolds stresses in the time-averaged transport equations. This is acceptable and provides prediction of temperature fields in case of fluids with a molecular Prandtl number (Pr) of about the unity. Since liquid metals are characterized by significantly lower Pr values, as a consequence of their high thermal conductivity, the previous analogy is not applicable and more advanced Turbulent Heat Transfer (THT)

* Corresponding author.
E-mail address: s.kenjeres@tudelft.nl (S. Kenjeres).

https://doi.org/10.1016/j.nucengdes.2020.110570
Received 27 July 2019; Received in revised form 7 February 2020; Accepted 9 February 2020

models can be required, Grotzbach (2013) and Roelofs et al. (2015). Considering the pool-type configuration of the MYRRHA reactor, typical flow patterns in large components (e.g. upper and lower plena) are characterized by multi-jet interactions. Hence, the jet flow was selected as a fundamental test case to be investigated. The current amount of reference data for wall-unconfined flows is still limited. In the open literature, only two relevant experiments are TEFLU and PLAJEST, in which single- and triple-jet liquid metal flows were investigated, respectively, Knebel et al. (1998) and Kimura et al. (2007). Related Direct Numerical (DNS) and Large-Eddy Simulations (LES) only counts a few examples too, Otić and Class (2007) and Tenchine et al. (2013). Despite the recent numerical studies on predicting momentum and passive scalar fields in forced jet flows (Le Ribault et al., 1999; Bogey and Bailly, 2009; Di Venuta et al., 2018), specific low-Pr fluid applications are still missing both experimentally and numerically.

In the present work, we compare the recently performed experiments (conducted at VKI within the MYRTE program funded by the European Commission) on a forced planar jet with heated co-flow with air (Pr = 0.71) and He-Xe gas mixture (Pr = 0.2), with RANS-based numerical simulations (performed at SCK•CEN and TUD). The aim is to compare standard Reynolds analogy-based approaches (Kader, 1981; Kays, 1994) and a more advanced low-Pr two-equation THT model, which was previously presented and solely validated with reference to the wall-confined flows (e.g. Manservisi and Menghini, 2014; Manservisi and Menghini, 2015; Da Via et al., 2016).

2. Experimental setup

The MYRTE wind tunnel was designed and operated at VKI to experimentally investigate a forced planar jet with heated co-flow and other fundamental test cases (e.g. backward-facing step). Air and He-Xe gas mixture were considered as working fluids with Pr = 0.71 and 0.2, respectively. Although the lowest Pr value is approximately one order of magnitude higher than the liquid metal range (e.g. LBE, Pr = 0.025), previous DNS studies on pipe flow at Pr = 0.2 demonstrated a sufficient impact on THT phenomena against air (Errico and Stalio, 2015). Moreover, a liquid metal experiment would have involved large difficulties in performing measurements of the turbulent quantities due to the opacity and high temperature of the fluid. A sketch of the experimental wind tunnel with a characteristic test section and Particle Image Velocimetry (PIV) set-up is shown in Fig. 1. Entering the jet convergent region, the co-flow was heated-up by two electrical resistances placed at either side of the planar jet. The resulting temperature difference between the co-flow and jet-flow was kept at $\Delta T = T_{CO} - T_J = 12$ K throughout the measurements. These temperatures were monitored by two fixed thermocouples at the end of both jet and co-flow entrainment regions. A third movable thermocouple, coupled to a hot-wire probe for velocity measurements, performed acquisition further downstream. Two porous plates upstream of the heaters were dimensioned to achieve a co-flow to jet velocity ratio of about $U_{CO}/U_J = 0.17$. Geometrical specifications of interest for the following numerical analyses are the jet-nozzle height of $h = 0.021$ m and global width of the test section of $W = 12.5$ h. Mean velocities at the inlet were $U_J = 16.01$ m/s and $U_{CO} = 2.67$ m/s. On the basis of these velocities, jet-nozzle height and kinematic viscosity of air at standard conditions, the Reynolds number of the jet was about 18000, confirming the forced convection regime, Buckingham (2018). In the present work, the measured first- and second-order statistics of flow and temperature will be used for comparison with simulations.

3. Numerical method

3.1. Governing equations

The steady-state RANS simulations were performed assuming a constant-property incompressible fluid and eddy viscosity/diffusivity

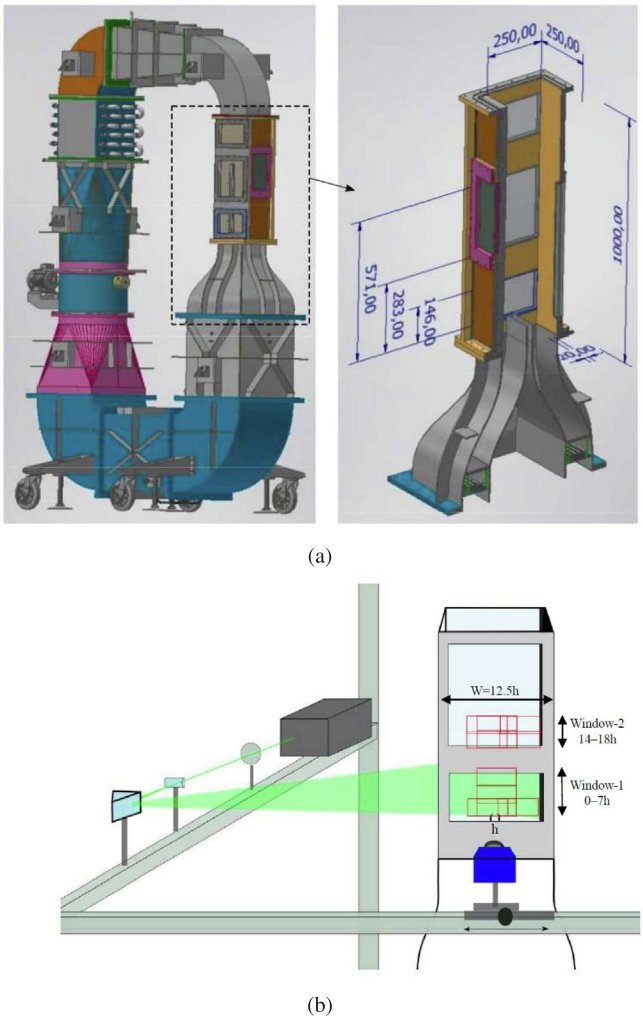

Fig. 1. Sketch of the MYRTE wind tunnel (a) and PIV experimental set-up (b).

hypotheses for turbulent transport. The Reynolds averaged velocity (U_i) and temperature (T) transport equations are:

$$\frac{\partial U_i}{\partial t} + U_j \frac{\partial U_i}{\partial x_j} = -\frac{1}{\rho}\frac{\partial p}{\partial x_i} + \frac{\partial}{\partial x_j}\left[(\nu + \nu_t)\frac{\partial U_i}{\partial x_j}\right] \quad (1)$$

$$\frac{\partial T}{\partial t} + U_j \frac{\partial T}{\partial x_j} = \frac{\partial}{\partial x_j}\left[(\alpha + \alpha_t)\frac{\partial T}{\partial x_j}\right] \quad (2)$$

where ν and α are the kinematic viscosity and thermal diffusivity of the fluid, respectively, whereas ν_t and α_t are the eddy viscosity and thermal diffusivity, Pope (2000).

3.2. Turbulence models

The standard $k-\varepsilon$ turbulence model is widely used in CFD to predict turbulent transport of momentum and different variants are currently available in industrial tools. It was also selected as a basic turbulence model in the present study. The additional transport equations of turbulent kinetic energy (k) and its dissipation rate (ε) are:

$$\frac{\partial k}{\partial t} + U_j \frac{\partial k}{\partial x_j} = P_k - \varepsilon + \frac{\partial}{\partial x_j}\left[\left(\nu + \frac{\nu_t}{\sigma_k}\right)\frac{\partial k}{\partial x_j}\right] \quad (3)$$

$$\frac{\partial \varepsilon}{\partial t} + U_j \frac{\partial \varepsilon}{\partial x_j} = \left(C_{\varepsilon_1} P_k - C_{\varepsilon_2}\varepsilon\right)\frac{k}{\varepsilon} + \frac{\partial}{\partial x_j}\left[\left(\nu + \frac{\nu_t}{\sigma_\varepsilon}\right)\frac{\partial \varepsilon}{\partial x_j}\right] \quad (4)$$

Table 1
Model coefficients of the $k-\varepsilon$ turbulence model.

C_μ	C_{ε_1}	C_{ε_2}	σ_k	σ_ε
0.09	1.44	1.92	1	1.3

where $P_k = \left[\nu_t\left(\frac{\partial U_i}{\partial x_j}+\frac{\partial U_j}{\partial x_i}\right)-\frac{2}{3}\delta_{ij}k\right]\frac{\partial U_i}{\partial x_j}$ represents the modeled production of turbulent kinetic energy. The eddy viscosity can now be defined as:

$$\nu_t = C_\mu \frac{k^2}{\varepsilon} \tag{5}$$

where σ_k, C_{ε_1}, C_{ε_2}, σ_ε and C_μ are model coefficients (Launder and Spalding, 1973) listed in Table 1. The standard wall functions were used for all turbulent quantities along the adiabatic walls.

The low-Reynolds variant of the $k-\varepsilon$ model is usually applied when more accurate predictions of the local wall-heat transfer is required, Jones and Launder (1972) and Manservisi and Menghini (2015). In the present work, we also consider such class of turbulence models. We selected $k-\varepsilon-\zeta-f$ turbulence model of Hanjalić et al. (2004) due to its numerical robustness and limited sensitivity to the grid non-uniformities. In this model, a velocity scale ratio $\zeta = \overline{v^2}/k$, replaced the original "wall-normal" velocity scale $\overline{v^2}$, which was previously proposed in Durbin (1995), Lien and Kalitzin (2001) and Kenjereš et al. (2005). The elliptic function f is also introduced in order to mimic separately the viscous wall-blocking effect. The final version of the model includes two additional transport equations:

$$\frac{\partial \zeta}{\partial t}+U_j\frac{\partial \zeta}{\partial x_j} = f-\frac{\zeta}{k}P_k-\varepsilon+\frac{\partial}{\partial x_j}\left[\left(\nu+\frac{\nu_t}{\sigma_\zeta}\right)\frac{\partial \zeta}{\partial x_j}\right] \tag{6}$$

$$L^2\nabla^2 f - f = \frac{1}{\tau}\left(C_1+C_2\frac{P_k}{\varepsilon}\right)\left(\zeta-\frac{2}{3}\right) \tag{7}$$

where σ_ζ, C_1 and C_2 are model coefficients, listed in Table 2. In contrast to the standard $k-\varepsilon$ models, both the length (L) and global dynamical time (τ) scales are now bounded by the Kolmogorov scales in combination with Durbin's realizability constraints as:

$$\tau = max\left[min\left(\frac{k}{\varepsilon},\frac{a}{\sqrt{6}C'_\mu|S|\zeta}\right),C_\tau\left(\frac{\nu}{\varepsilon}\right)^{\frac{1}{2}}\right] \tag{8}$$

$$L = C_L max\left[min\left(\frac{k^{\frac{3}{2}}}{\varepsilon},\frac{k^{\frac{1}{2}}}{\sqrt{6}C'_\mu|S|\zeta}\right),C_\eta\left(\frac{\nu^3}{\varepsilon}\right)^{\frac{1}{4}}\right] \tag{9}$$

where S is the stress-strain tensor, while a, C_τ, C_η and C_L are model coefficients reported in Table 2. Finally, the eddy viscosity can be defined as:

$$\nu_t = C'_\mu \zeta k \tau \tag{10}$$

with C'_μ as a model coefficient. The boundary conditions used in the elliptic-relaxation based turbulence models are as follows: zero-values were imposed to ν_t, k and ζ, while $\varepsilon = 2\nu k/\delta^2$ and $f = -2\nu\zeta/\delta^2$, where δ is the wall distance. It is expected that the more advanced $k-\varepsilon-\zeta-f$ model will predict more accurately the near-wall phenomena when compared to the standard $k-\varepsilon$ model employing the wall-functions. On the other hand, the numerical mesh needs to be refined to get the characteristic non-dimensional wall distance less than one, which will significantly increase the computational costs. For flows in the non-confined geometries, such as in the present planar jet with heated co-flow, it is interesting to compare these two approaches, especially in the jet-spreading region, where the wall effects are diminishing.

Table 2
Model coefficients of the $k-\varepsilon-\zeta-f$ turbulence model.

C'_μ	C'_{ε_1}	C'_{ε_2}	σ_ζ	a	C_τ	C_η	C_L
0.22	$1.4\left(1+\frac{0.012}{\zeta}\right)$	1.9	1.2	0.6	6	85	0.36

3.3. Turbulent heat transfer models

The simplest way of modeling of the turbulent heat flux is to apply so called "simple-gradient hypothesis", as follows:

$$\overline{\theta u_i} = -\alpha_t\frac{\partial T}{\partial x_i} \tag{11}$$

where the eddy diffusivity (α_t) is calculated through the Reynolds analogy:

$$\alpha_t = \frac{\nu_t}{\mathrm{Pr_t}} \tag{12}$$

In the present work, two values of the turbulent Prandtl number are considered: the standard value ($\mathrm{Pr}_t = 0.85$) and the value recommended for the low-Prandtl fluids ($\mathrm{Pr}_t = 2$), Grotzbach (2013). Departing from this constant-value approach, Pr_t-correlations for low-Prandtl fluids are also available in the literature. One of the most popular is so-called Kays correlation derived from the series of experimental data on pipe and duct flows for various values of Prandtl number, Kays (1994):

$$\mathrm{Pr_t^{Kays}} = 0.85+\frac{2}{\frac{\nu_t}{\nu}\mathrm{Pr}} \tag{13}$$

Another approach in modeling of the turbulent heat flux is to use additional transport equations for energy of the temperature fluctuations (temperature variance, k_θ) and its dissipation rate (ε_θ), e.g. (Abe et al., 1995; Hanjalić et al., 1996; Kenjereš and Hanjalić, 2000; Manservisi and Menghini, 2014), which eliminates necessity to define the turbulent Prandtl number. Here, we will apply a recent low-Prandtl $k-\varepsilon-k_\theta-\varepsilon_\theta$ model of Manservisi and Menghini (2015), which was extensively validated for the wall-confined flows:

$$\frac{\partial k_\theta}{\partial t}+U_j\frac{\partial k_\theta}{\partial x_j} = \frac{\partial}{\partial x_j}\left[\left(\alpha+\frac{\alpha_t}{\sigma_{k_\theta}}\right)\frac{\partial k_\theta}{\partial x_j}\right]+P_{k_\theta}-\varepsilon_\theta \tag{14}$$

$$\frac{\partial \varepsilon_\theta}{\partial t}+U_j\frac{\partial \varepsilon_\theta}{\partial x_j} = \frac{\partial}{\partial x_j}\left[\left(\alpha+\frac{\alpha_t}{\sigma_{\varepsilon_\theta}}\right)\frac{\partial \varepsilon_\theta}{\partial x_j}\right] + (C_{p_1}P_{k_\theta}-C_{d_1}\varepsilon_\theta)\frac{\varepsilon_\theta}{k_\theta}+(C_{p_2}P_k-C_{d_2}\varepsilon)\frac{\varepsilon_\theta}{k} \tag{15}$$

where $P_{k_\theta} = \alpha_t\left(\frac{\partial T}{\partial x_j}\right)^2$ is the production term of temperature variance (k_θ), while σ_{k_θ}, $\sigma_{\varepsilon_\theta}$, C_{p_1} and C_{p_2} are model coefficients, listed in Table 3. The remaining C_{d_2} coefficient is a function of the turbulent Reynolds number (defined as $R_t = k^2/(\varepsilon\nu)$) and normalized wall distance (defined as $R_\delta = \delta(\varepsilon\nu)^{1/4}/\nu$) and is calculated as:

$$C_{d_2} = [1.9(1-0.3e^{-0.0237R_t^2})-1](1-e^{-0.1754R_\delta})^2 \tag{16}$$

The eddy diffusivity is defined as:

$$\alpha_t = C_\theta k \tau_{l_\theta} \tag{17}$$

where C_θ is model coefficient reported in Table 3, and τ_{l_θ} is the local thermal characteristic time scale calculated as:

$$\tau_{l_\theta} = (f_{1_\theta}B_{1_\theta}+f_{2_\theta}B_{2_\theta}) \tag{18}$$

Table 3
Model coefficients of the $k_\theta-\varepsilon_\theta$ heat transfer model.

C_θ	C_{p_1}	C_{p_2}	C_{d_1}	B_∞	σ_{k_θ}	$\sigma_{\varepsilon_\theta}$	C_γ
0.1	0.925	0.9	1	0.9	1.4	1.4	0.3

which consists of the asymptotic, mixed and local contributions, implicitly defined as:

$$f_{1\theta} = (1 - e^{-0.0526R_\delta\sqrt{\mathrm{Pr}}})(1 - e^{-0.0714R_\delta}) \tag{19}$$

$$B_{1\theta} = \tau_u B_\infty \tag{20}$$

$$f_{2\theta}B_{2\theta} = \tau_u\left(f_{2a\theta}\frac{2R}{R + C_\gamma} + f_{2b\theta}\sqrt{\frac{2R}{\mathrm{Pr}}}\frac{1.3}{\sqrt{\mathrm{Pr}}\,\mathrm{R_t}^{3/4}}\right) \tag{21}$$

$$f_{2a\theta} = f_{1\theta}\,e^{-4\cdot10^{-6}R_t^2} \tag{22}$$

$$f_{2b\theta} = f_{1\theta}\,e^{-2.5\cdot10^{-5}R_t^2} \tag{23}$$

where C_γ and B_∞ are constants also reported in Table 3. Here, the time-scale ratio is defined as $R = \tau_\theta/\tau_u$, with the global dynamical time scale $\tau_u = k/\varepsilon$, and the global thermal time scale $\tau_\theta = k_\theta/\varepsilon_\theta$. The boundary conditions at the wall are zero values of k_θ and α_θ, whereas zero-gradient is applied for ε_θ.

3.4. Computational code

The OpenFOAM-2.4.0 CFD code was used to perform the RANS simulations. All numerical simulations were executed in the steady mode. This steady mode approach proved to be appropriate because of the strong stabilizing effect of the imposed co-flow in the closed test section, which practically eliminated a typical oscillatory behavior of plumes and other forced convection jets, Fregni et al. (2019). This was additionally proven by ability to get a fully convergent solutions for all performed simulations, which will be impossible if any kind of the oscillatory behavior will be triggered. The simulations were performed by using the SIMPLE algorithm for coupling between the velocity and pressure fields. The second-order central differencing scheme was used to discretize the gradient and Laplacian terms, whereas the second-order TVD scheme was used for the divergence terms, Versteeg and Malalasekera (1995). The steady simulations were performed with typical under-relaxation parameters of 0.1 for the pressure, 0.3 for the velocity and 0.5 for all remaining turbulence variables. The convergence criterion of 10^{-8} was applied (and achieved) for all variables.

3.5. Computational domain and boundary conditions

The experimental test section was represented using two computational domains and three different numerical meshes, Fig. 2. It was decided to generate three-dimensional symmetrical domains in order to have a universal configuration which can be used also for initialization of velocity and temperature fields, as well as to check the required numerical resolution of a high-fidelity CFD approach (Large Eddy Simulation) (the follow-up numerical study).

The first computational domain (defined as 'D1') was designed to be as simple as possible. It is starting at the nozzle outlet plane of the experimental setup, which makes it possible to simply prescribe measured profiles of the velocity and turbulence kinetic energy. This option is also used to mimic some experimentally observed imperfections (in terms of the asymmetrical distributions of the incoming flow, which will have a significant impact on the flow profiles in the jet mixing zone). These can be investigated further by modeling the actual shape of the curved inlet segment of the experimental wind tunnel, but this was not considered in the present work.

The second computational domain (defined as 'D2') was created to achieve a more universal description of planar jet flow, estimating possible design-specific deviations from the theoretical behavior (e.g. unbalanced co-flows at the jet side). In the 'D2' configuration, three periodic channels were set as the pre-cursor simulation domains in order to provide the fully developed flows before entering the jet-mixing zone. The special attention was devoted to obtaining the desired characteristic ratio between the velocity magnitude of the central jet and its co-flow counterparts. This was achieved by taking the most uniform co-flow side from experiments (the left side) with the mean inlet velocity of 3.15 m/s, which was set to both co-flow inlets. Then, the mean jet velocity is imposed to be 14.97 m/s to ensure the total flow rate balance. Expectations were to get a reasonable agreement with experimental data mainly in the left-side and in the center of the jet.

The coordinate system in the numerical model of the experimental test section was oriented in such a way that U, V, and W represent the velocity components in streamwise (x), crosswise (y) and spanwise (z) directions, respectively. Gravity effects were neglected considering the high Reynolds number of the jet (experimentally, about 18000), which also leads to a Richardson number much lower than the unity.

Both working fluids (air and He-Xe gas mixture) were assumed to have a constant kinematic viscosity, $\nu = 1.55\cdot10^{-5}$ m^2/s, whereas the thermal properties assumed molecular Prandtl numbers of 0.71 and 0.2, respectively. Fixed-scalar inlet conditions were set for temperature in both domains. In case of air, co-flow and jet inlet temperatures were $T_{CO} = 311.1$ K and $T_J = 299.1$ K, respectively. In case of the He-Xe gas mixture, they were $T_{CO} = 307.5$ K for the co-flow and $T_J = 295.5$ K for the jet. These values resulted from the monitoring of experimental inlet conditions, showing that the target temperature difference of $12K$ was actually maintained during the MYRTE wind tunnel operation. Finally, turbulent quantities were also imposed as uniform fixed-scalar values at the channels inlet of pre-cursor simulations (only for the very first iteration) of domains D2 and D2.1, e.g. $k^{in} = 1.5(I_t\ \overline{U})^2$, with $\overline{U}$ is the mean velocity (obtained from PIV), $I_t = 0.1$ is the turbulence intensity, and $\varepsilon^{in} = (C_\mu^{3/4}(k^{in})^{3/2})/0.07h$ is the dissipation rate of the turbulent kinetic energy. Note that the cyclic-boundary conditions were imposed in the pre-cursor simulations, which are then mapped onto the planes before the inlets of mixing-jet region (the pre-cursor domains with

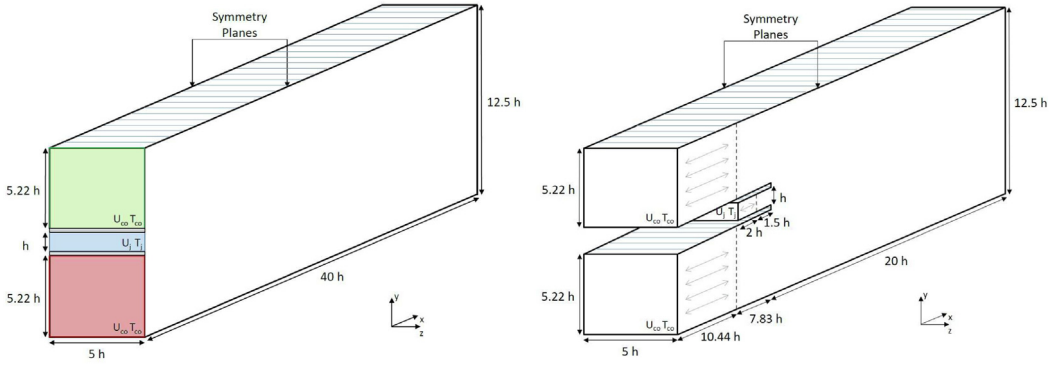

(a) (b)

Fig. 2. Sketch of the computational domains D1 (a) and D2/D2.1 (b).

lengths of 10.44 h for the co-jets and of length 2 h for the central-jet are indicated by arrows in Fig. 2b.) For the temperature variance and its dissipation rate, following values are imposed, $k_\theta = 10^{-3}$ K^2, and $\varepsilon_\theta = 10^{-3}$ K^2/s, respectively.

The remaining boundary conditions were analogously set in both domains D1 and D2. The crosswise-normal surfaces were defined as no-slip adiabatic walls. The spanwise-normal patches were defined as symmetry planes. The outlet boundary condition was set to zero-gradient for velocity and turbulent quantities. A zero-gradient inlet condition was also set for the pressure while this was fixed at a reference value of zero at the outlet.

3.6. Mesh details

Three different meshes were generated as a consequence of the selected turbulence models. In domains D1 and D2, the standard $k-\varepsilon$ model was solely used (i.e. the high-Reynolds model with wall-functions) while the $k-\varepsilon-\zeta-f$ was tested in a domain D2-variant (D2.1) (i.e. the low-Reynolds model with integration up to the wall). The D2.1 configuration is geometrically identical to the D2, but with a significantly finer numerical mesh in the proximity of walls. To better visualize differences from meshes in domains D2 and D2.1, Fig. 3 shows details around the jet nozzle. The most important mesh specifications are collected in Tables 4 and 5. In addition to the partial (in the jet-spreading and co-flow regions) and the total amount of control volumes, additional information containing the characteristic non-dimensional wall distance (y^+) and typical mean cell length (l_c, which was defined as the cubic-root of the ratio between the total volume of specific subdomain and number of the control volumes in that region, providing an indication of the isotropic mesh element size). To verify the initial formation of the mixing layer, additional mesh sensitivity analyses were also performed by doubling the number of control volumes in the streamwise direction (which are indicated with '(f)').

4. Results and discussion

4.1. Qualitative analysis of flow and temperature fields

In order to provide a qualitative analysis of the planar jet flow behavior at Pr = 0.2 (He-Xe gas mixture), contour plots in the central (x, y)-plane for domain D2.1 are presented in Figs. 4–6. Note that all plots are extracted from results obtained by the most comprehensive low-Reynolds models, using the $k-\varepsilon-\zeta-f$ for the flow fields and $k_\theta-\varepsilon_\theta$ for thermal fields. We start our analysis with a presentation of typical flow and turbulence parameters associated with the velocity field. The contours of the velocity magnitude show a centrally located plane jet, which is additionally stabilized by the co-flow jets (which are just slightly visible due to rather small flow ratio $U_{CO}/U_J = 0.14$), Fig. 4(a). This strong shear between the central and co-flow jets is the major source of the turbulence kinetic production, which can be observed from contours of the turbulence kinetic energy in Fig. 4(b). The global dynamical time scale ($\tau_u = k/\varepsilon$) distribution, shown in Fig. 4(c), portrays that the central jet region (where the turbulent diffusion is the dominant mechanism) and the edges of the central jet (where the shear-production is dominant mechanism) are characterized by the smallest length-scales at which dissipation of turbulence takes place. The contours of the parameter ($\zeta = \overline{v^2}/k$), are plotted in Fig. 4(d). Note that ($\overline{v^2}$) should be analyzed as the intensity of the velocity fluctuations perpendicular to the flow direction, and is reduced to its classical definition of the normal turbulent-stress component in the proximity of the wall. Next to small regions close to the inlet plane (resulting from the incoming wall-bounded channel), the strongest deviation of $\overline{v^2}$ from the total turbulence kinetic energy ($k = 0.5(\overline{u_i u_i})$) coincides with strong-shear regions.

Distributions of the mean temperature and temperature variance show a similar trend as for the velocity field counterparts, Figs. 5(a) and (b). On first sight, it can be surprising considering the low value of the Prandtl number (Pr = 0.2), which should lead to the different dynamic behavior of the velocity and thermal fields. On another hand, the considered case is strongly dominated by the forced convection, which makes the molecular contributions to the heat flux almost negligible in the central part of the jet. The differences between the temperature variance (Fig. 5) and turbulent kinetic energy (Fig. 4(b)) are more pronounced. The former one shows the highest values in the proximity of the inlet, with a diminishing trend as the central jet is developing, whereas the latter one shows the consistent behavior. The contours of the global thermal time-scale are shown in Fig. 5(c). It can be seen that contours show a similar distribution to the previously analyzed global dynamical time-scale (shown in Fig. 4(c)), with the smallest values in the center and along edges of the jet. Finally, contours of the turbulent Prandtl are plotted in Fig. 5(d). Here, the turbulent Prandtl number is evaluated (by combining Eqs. (10) and (17)) as:

Table 4
Mesh details of the jet-spreading region from the different computational domains.

	N_x	N_y	N_z	*Total*	$l_c[mm]$
D1	120	141	11	186.1k	4.94
D2	36	113	11	44.8k	6.3
D2.1	46	283	21	273.4k	3.45

Table 5
Mesh details of the periodic jet and co-flow channels in domains D2 and D2.1.

	N_x^J	N_y^J	N_x^{CO}	N_y^{CO}	N_z	$Total^{Jet}$	$Total^{Coflow}$	y^{+Jet}	$y^{+Coflow}$
D2	14	17	29	44	11	2.6k	14k	22	11
D2.1	28	67	58	62	21	39.4k	75.5k	0.5	0.9

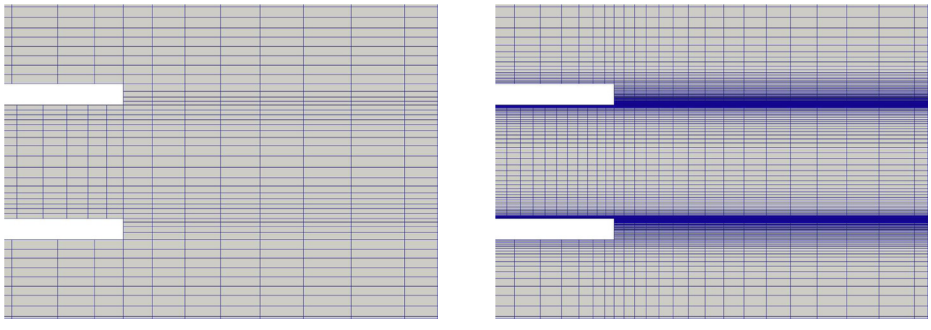

(a) (b)

Fig. 3. Mesh details at the inlet from computational domains D2 (a) and D2.1 (b).

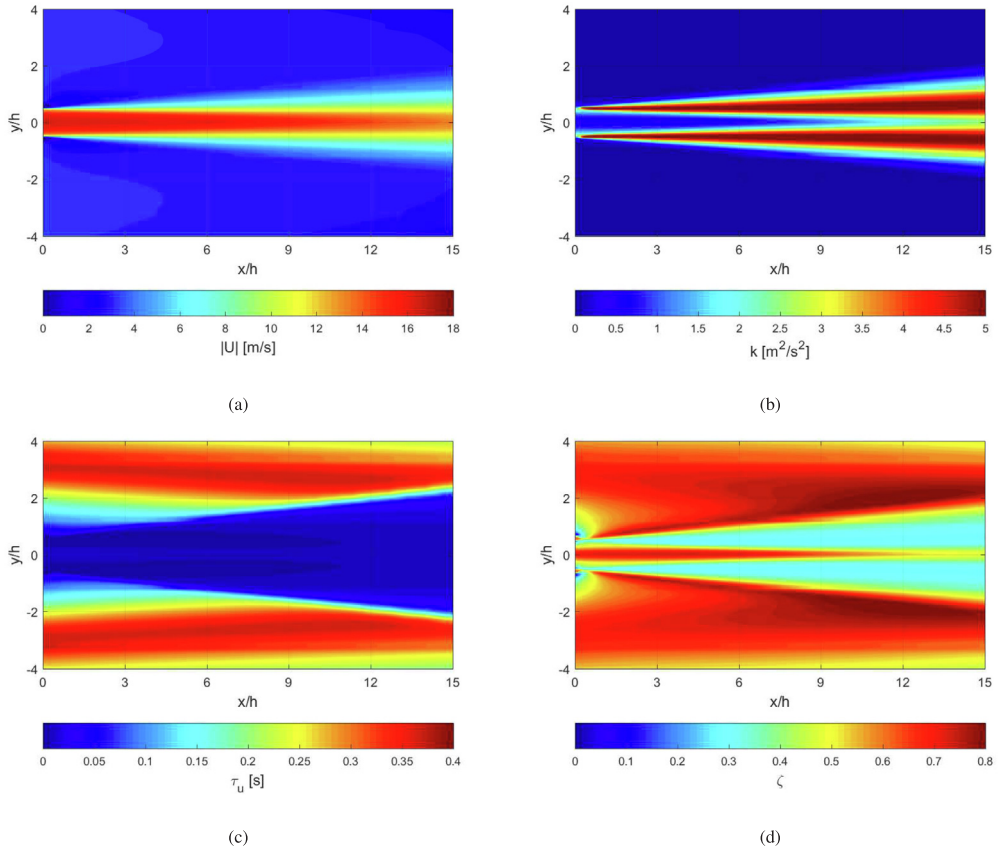

Fig. 4. Contours of velocity magnitude (a), turbulent kinetic energy (b), global dynamical time-scale (c) and velocity-scale ratio (d) from the low-Reynolds $(k-\varepsilon-\zeta-f)+(k_\theta-\varepsilon_\theta)$ turbulence model (domain D2.1).

$$\mathrm{Pr_t}=\frac{\alpha_t}{\nu_t}=\frac{C_\theta\ k\ \tau_{l_\theta}}{C'_\mu\ \overline{v^2}\ \tau} \tag{24}$$

It can be seen that a strongly non-uniform distribution of $\mathrm{Pr_t}$ is obtained (similarly to Chua and Antonia (1990)), with values varying in the 0.2–2 range. The lower values of the $\mathrm{Pr_t}$ are obtained in regions bounded with the shear-layers and central jet, indicating the regions where the turbulent thermal diffusion dominates over the turbulent momentum diffusion. Finally, Fig. 6 shows the ratio between turbulent and molecular viscosity (a) and diffusivity (b). It can be seen that this ratio is significantly larger for the momentum transfer compared to its thermal counterpart.

4.2. Quantitative analysis of the flow field

We will consider next a detailed comparative assessment between the PIV measurements and numerical simulations. The streamwise velocity and turbulent kinetic energy were normalized by characteristic difference between the inlet jet- and co-flow velocities (defined as $\Delta U=U_J-U_{CO}$). Since two-dimensional PIV measurements were performed, the streamwise ($\overline{uu}$) and crosswise ($\overline{vv}$) turbulent stress components are directly available. The total turbulent kinetic energy is estimated as $k_{\mathrm{PIV}}=0.5(\overline{uu}_{\mathrm{PIV}}+\overline{vv}_{\mathrm{PIV}}+\overline{ww})$, with $\overline{ww}=2/3\overline{vv}_{\mathrm{PIV}}$ (Pope, 2000), and this value is used for comparisons with RANS results.

We evaluate first the inlet profiles of the non-dimensional streamwise velocity and turbulent kinetic energy profiles for the 'central jet of D2 and D2.1' configurations, in order to check that fully developed turbulence profiles are obtained, Fig. 7. Note that 'D2' indicates coarser mesh and application of the high-Reynolds turbulence model, while 'D2.1' indicates a refined numerical mesh with integration up to the wall of the low-Reynolds turbulence model. The profiles are extracted at $x/h=-2.5$, i.e. at the half-length of the periodic channels. It can be concluded that for both RANS models a good agreement is obtained for the non-dimensional streamwise velocity in comparison with the DNS data of Moser et al. (1999), Fig. 7(a). In contrast to that, profiles of the turbulent kinetic energy reveal that high-Reynolds variant of the model is not able to accurately predict the near-wall behavior, with a significant under-prediction of the characteristic peak, Fig. 7(b). This is in accordance with a known deficiency of the standard high-Reynolds $k-\varepsilon$ model of Launder and Spalding (1973). Prediction of the low-Reynolds $k-\varepsilon-\zeta-f$ RANS model shows significant improvement and overall good agreement with the DNS profiles of the turbulent kinetic energy. This improvement is due to the accurate prediction of the wall-blockage effect included through the elliptic-relaxation approach. Additional mesh sensitivity analysis is performed by doubling the number of control volumes in the x-direction (as indicated by '(f)'). It can be seen that the obtained results are grid-independent. The same validation exercise was also performed in case of the periodic co-flow channels providing an analogous result, i.e. the fully developed turbulence profiles were obtained.

The profiles of the non-dimensional streamwise velocity and turbulent kinetic energy exactly at the inlet plane (at $x/h=0$) are shown in Fig. 8. It is obvious that experimental data are showing asymmetrical distributions ('D1' domain), caused by some constraints of the experimental setup, which include a presence of internal components and a convergent-shape of co-flow channels. The extended simulation domain results (with pre-cursor simulation to get fully developed profiles) exhibit, as expected, symmetrical profiles ('D2' and 'D2.1' domains). It should be noted that differences between the 'D1' and 'D1(f)' profiles are due to the sampling settings in OpenFOAM, since the values in the centers of control volumes are used instead of their cell-faces. Consequently, results obtained in 'D1(f)' domain show a better agreement

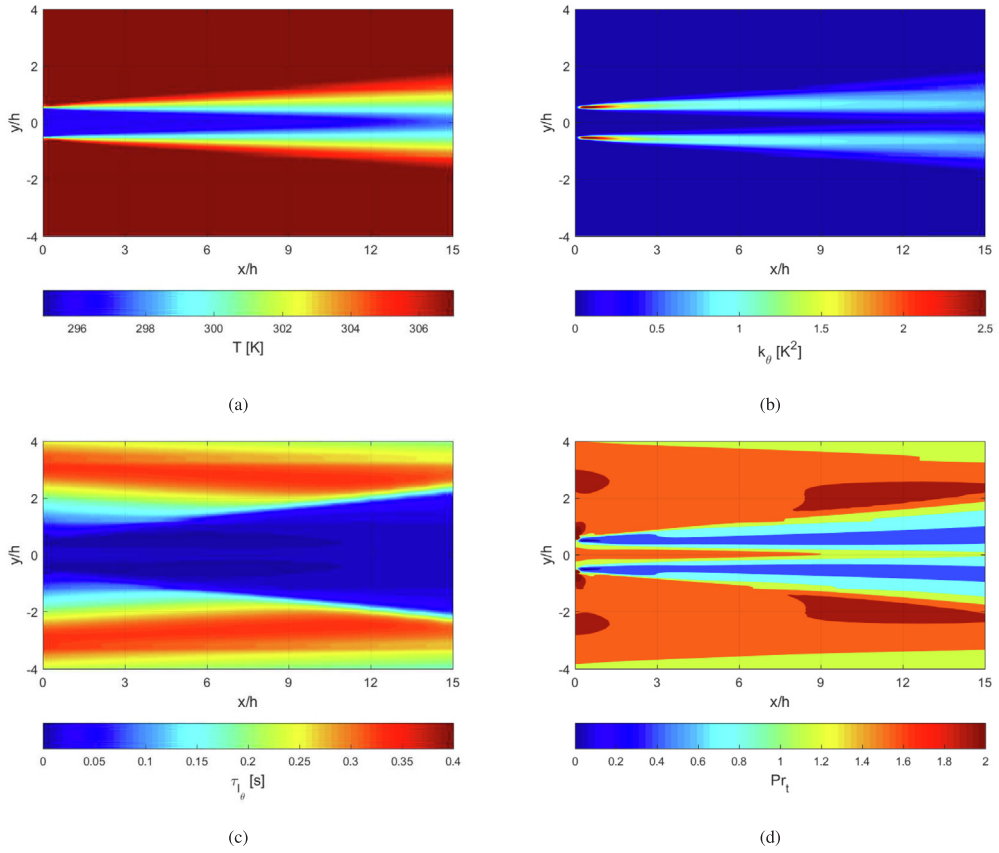

Fig. 5. Contours of temperature (a), temperature variance (b), local thermal time scale (c) and turbulent Prandtl number (d) at Pr = 0.2, obtained from the low-Reynolds $(k-\varepsilon-\zeta-f)+(k_\theta-\varepsilon_\theta)$ turbulence model (domain D2.1).

with experiments at $y/h = 0.5$ and $y/h = -0.5$ locations due to their smaller distance of the first row of control volumes from the inlet plane in comparison to 'D1' domain, Fig. 8(a). It can be also seen that the low-Reynolds RANS model ('D2.1') captures the best characteristic wakes at the nozzle near-wall regions (located in the proximity of above mentioned $y/h = 0.5$ and -0.5 locations). The profiles of non-dimensional turbulent kinetic energy show larger differences between simulations and experiments, Fig. 8(b). In addition to already mentioned asymmetrical behavior, there is also a significant difference in predicting the characteristic peaks, indicating that simulated fully developed inflows are underpredicting the turbulence intensity in the co-flow channels, whereas its intensity in the central-jet inflow is overpredicted - independently on used turbulence model (i.e. for both high- ('D2') and low-Reynolds model ('D2.1'), respectively). This low intensity of turbulence in the central jet can be partially explained by partial laminarization effects due to nozzle constriction, as discussed in Back et al.

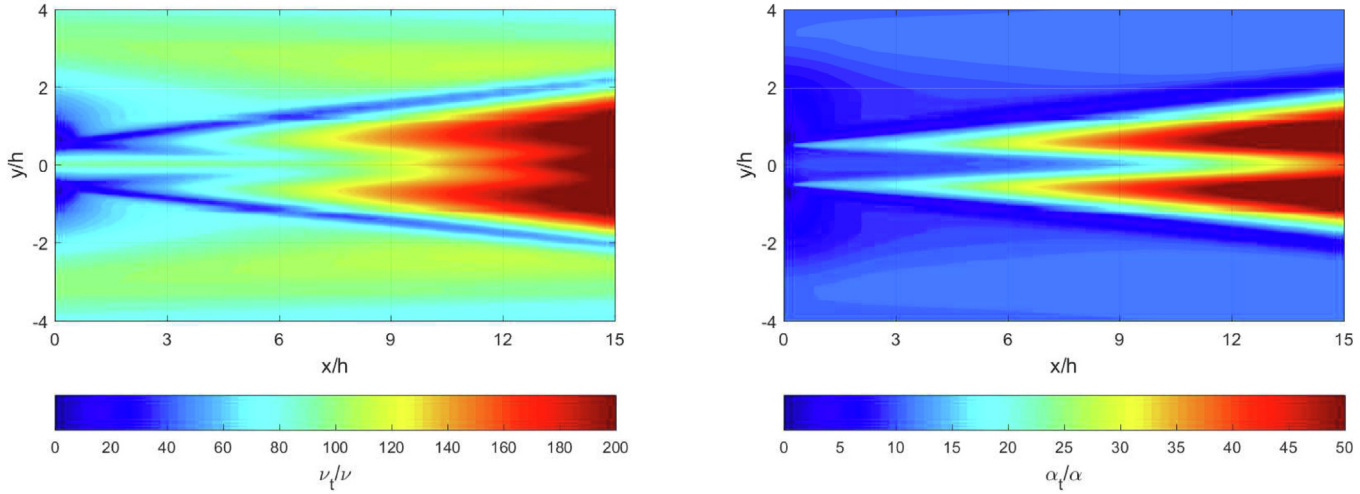

Fig. 6. Contours of turbulent to molecular viscosity (a) and diffusivity (b) ratios at Pr = 0.2, obtained from the low-Reynolds $(k-\varepsilon-\zeta-f)+(k_\theta-\varepsilon_\theta)$ turbulence model (domain D2.1).

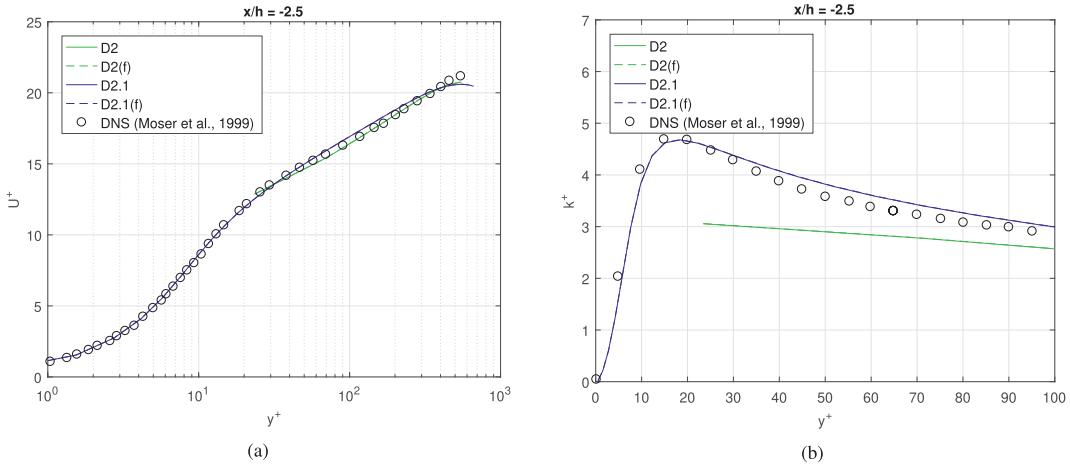

Fig. 7. Universal log-law profiles of velocity (a) and turbulent kinetic energy (b) as jet inlet conditions in domain D2 (the high-Reynolds turbulence model) and D2.1 (the low-Reynolds turbulence model). Note that (f) indicates the mesh refinement with a factor two in the streamwise direction.

(1970). The effects of the experimentally observed asymmetrical distributions and symmetrical fully developed turbulence conditions will be compared at different streamwise locations, $x/h = 3, 5, 7$, respectively, Fig. 9. At $x/h = 3$ location, the peak of the central jet velocity, as well as it is cross-wise spreading show an overall good agreement with experiments, Fig. 9(a). The low-Reynolds RANS model results ('D2' and 'D2.1') show a slight overprediction for the upper co-flow region ($y/h > 0$). At the same location, the numerically predicted non-dimensional turbulent kinetic energy profiles show significant underprediction in the central jet region for both models, Fig. 8(b). It is surprising that the PIV data exhibit behavior with identical peaks, despite the non-symmetrical trends at $x/h = 0$. Agreement with PIV measurements is better in the co-flow regions for the high-Reynolds model ('D1' and 'D1(f)') results.

The low-Reynolds model ('D2.1') shows the best agreement with measurements for the mean streamwise velocity component at $x/h = 5$ location, Fig. 9(c). The only deviation is obtained for the upper co-flow region. The high-Reynolds model ('D1') shows better prediction in this upper co-flow region, but cross-wise spreading is significantly underpredicted. Agreement between measurements and simulations of TKE profiles at this location is much better, as shown in Fig. 9(d). The peak values are well predicted with all models. The high-Reynolds model ('D1') shows good agreement in the co-flow regions, but underpredicts the level of TKE in the jet center. With further increase of the distance from the inlet plane, $x/h = 7$, the experimentally observed asymmetry in the upper co-flow region increases for both velocity and TKE profiles, Fig. 9(e) and (f). The velocity peak value is again well predicted with all models, Fig. 9(e). The TKE profiles indicate that the low-Reynolds ('D2.1') model shows the good prediction of the peaks, whereas the high-Reynolds ('D1') model is closest to PIV in the co-flow regions, Fig. 9(f). The profiles of the normalized turbulent shear stress component ($\overline{uv}$) at characteristic locations are shown in Fig. 10. The shear turbulent stress component prediction is important since it makes the most important source in the production of the turbulent kinetic energy. It can be seen that the asymmetrical distribution is again predicted better with the experimentally adjusted turbulent inlet for the high-Reynolds $k - \varepsilon$ model.

In summarizing the quantitative analysis of the flow field, an overall good agreement between PIV measurements and RANS simulations is obtained. The cross-wise profiles of the mean streamwise velocity at different locations downstream from the inlet plane show a good prediction of the characteristic peak values in the center of the jet. Also, the jet spreading is well captured too. Similarly, the simulated cross-wise profiles of the turbulent kinetic energy show a proper behavior with two characteristic peaks caused by strong shear between the central and co-flow jets. The experimental data of TKE in comparison with the numerical results indicate more rapid decay of the peak values of TKE in the streamwise direction. An additional attempt is made to mimic more closely asymmetrical distributions of measured profiles. It is shown that experimentally obtained differences between the upper and lower co-flow regions can be reasonably predicted by imposing corresponding inlet profiles for mean velocity and turbulent kinetic energy.

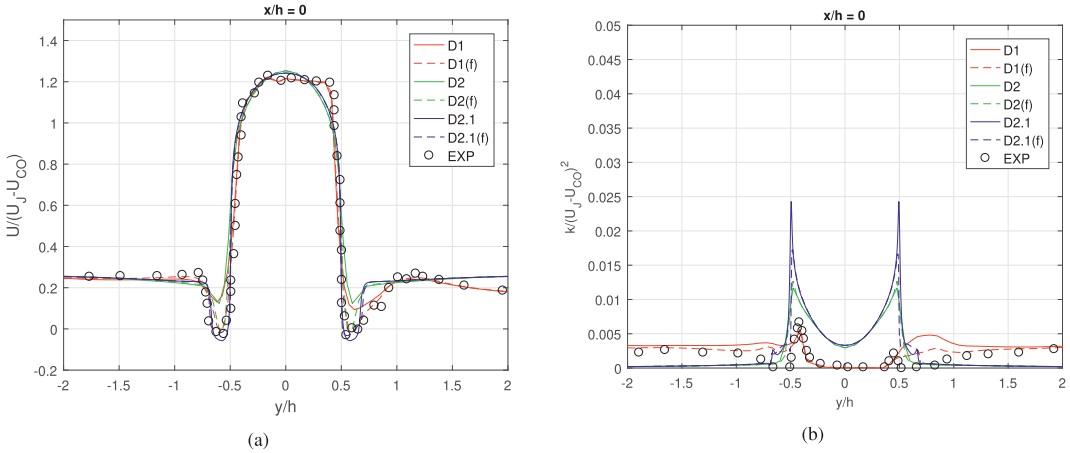

Fig. 8. Profiles of normalized streamwise velocity (a) and turbulent kinetic energy (b) at the jet inlet.

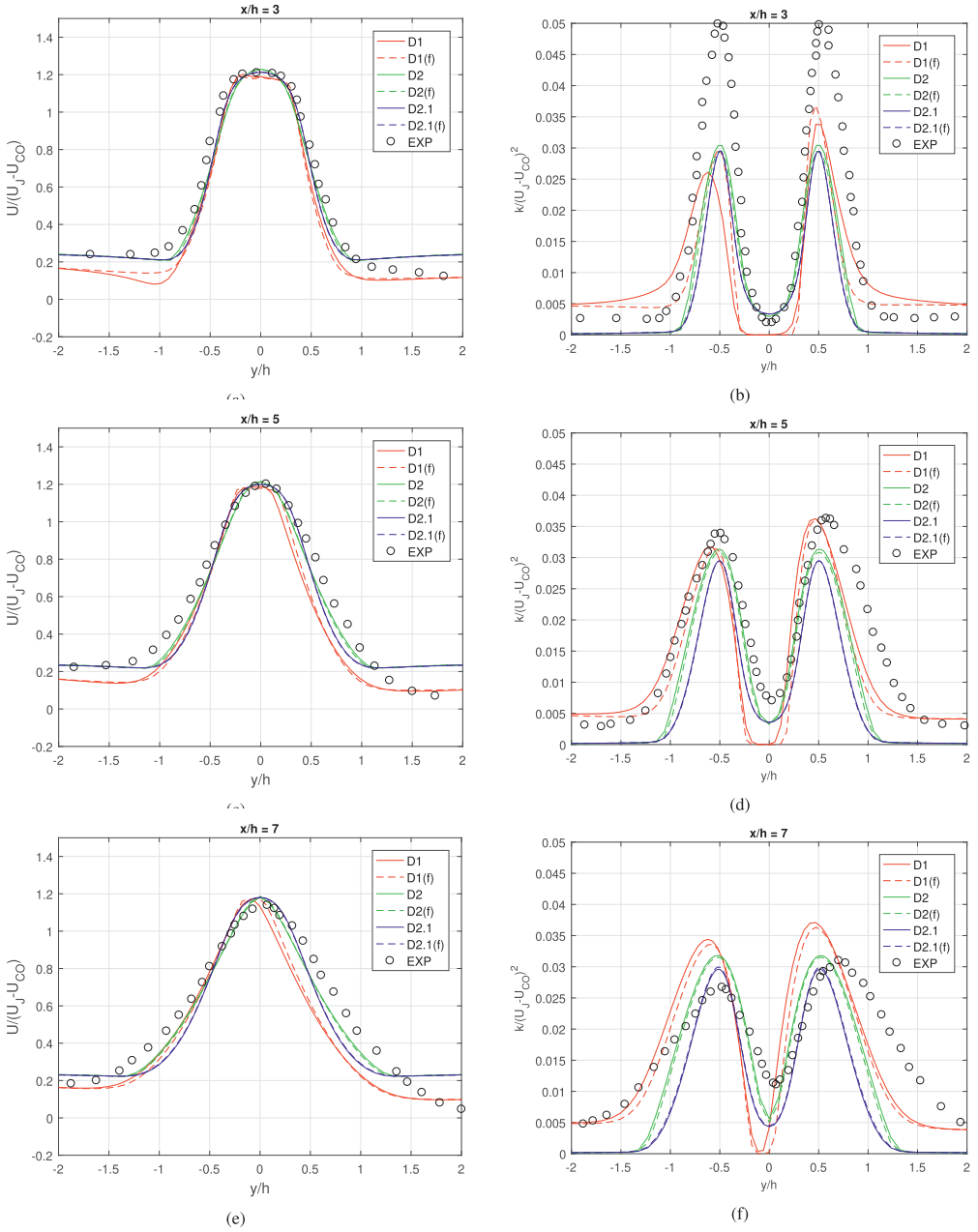

Fig. 9. Profiles of normalized streamwise velocity (a, c, e) and turbulent kinetic energy (b, d, f) at different locations.

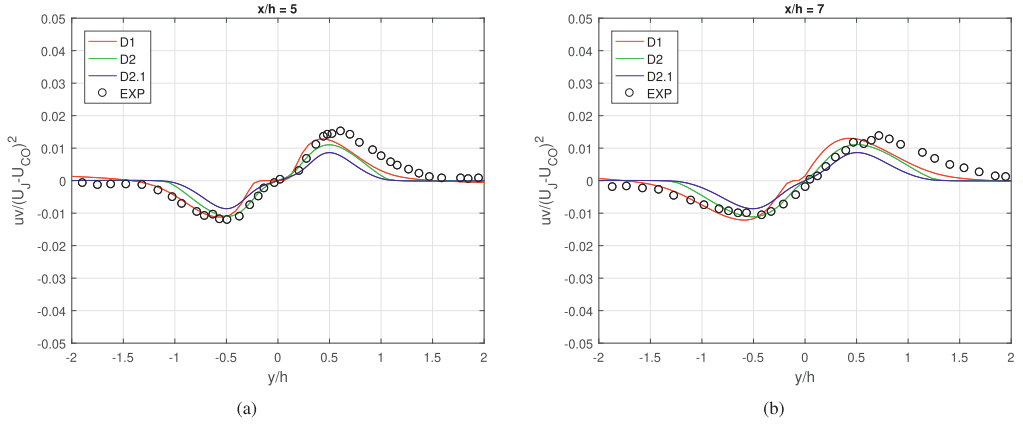

Fig. 10. Profiles of normalized turbulent shear stress component ($\overline{uv}$) at different locations (a, b).

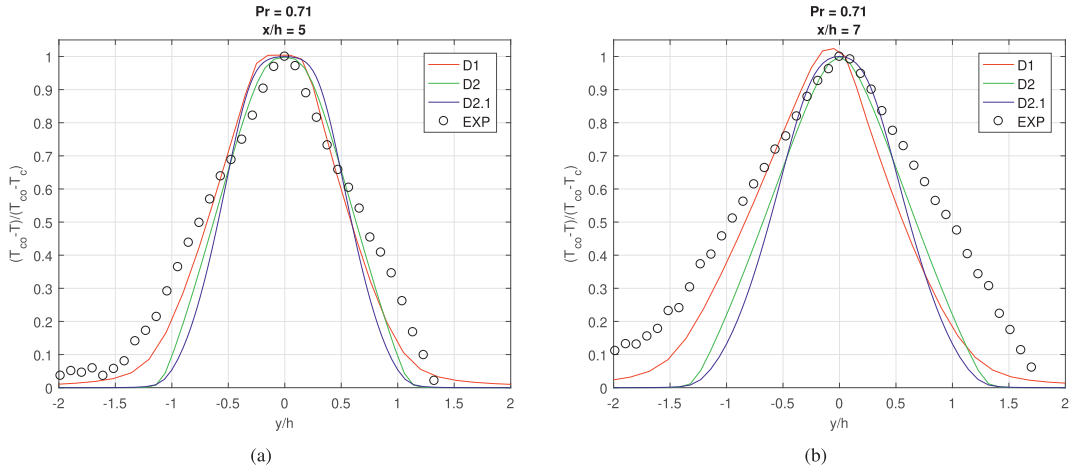

Fig. 11. Profiles of normalized temperature at Pr = 0.71 and Pr_t = 0.85 from domains D1, D2 and D2.1 at different locations (a, b).

4.3. Quantitative analysis of the thermal field

Furthermore, we perform a comparison between measured and numerically obtained mean temperature profiles for two different values of Prandtl number at two locations, $x/h = 5$ and 7, respectively, Figs. 10 and 11. During experiments, it was observed that the mean temperature of the working fluid was slightly increased in time. This increase resulted in a time-dependent behavior of the jet and co-flow inlet temperatures. To eliminate these time-dependencies, the mean temperature was non-dimensionalized as: $T^* = (T_{CO} - T)/(T_{CO} - T_c)$, with T_c as the centerline temperature. Note that a constant uniform inlet temperature profiles of the central jet and co-flows were specified for all numerical simulations. For the air as working fluid case, a simple Reynolds analogy in the modeling of the turbulent heat flux is applied with the characteristic values of the turbulent Prandtl number of Pr_t = 0.85. It can be seen that a reasonable agreement is obtained with experimental data at both locations, Fig. 11. The agreement is best for the 'D1' model where the asymmetrical inlets are imposed, although the cross-wise spreading is still underpredicted compared to the experiments.

For the low-Prandtl working fluid case (Pr = 0.2), various approaches in modeling the turbulent heat flux are tested, including: (i) the Reynolds analogy with two values of the turbulent Prandtl number (Pr_t = 0.85 and 2, respectively), (ii) the Prandtl number is evaluated from Kays correlation, and finally (iii) the full six-equation low-Reynolds model $k - \varepsilon - \zeta - f - k_\theta - \varepsilon_\theta$ model, which does not require specification of the Pr_t. From the non-dimensional temperature profiles at $x/h = 5$ and 7, it can be concluded that more accurate modeling of the turbulent heat flux does not bring many differences, Fig. 12. The agreement between simulations and experiments is poor. The experiments indicate significantly wider and asymmetrical distributions outside the $-0.5 \leqslant y/h \leqslant 0.5$ region, whereas the numerical simulations exhibit theoretically more proper Gaussian-like profiles, which were also reported in experimental studies of Franco-Medrano et al. (2017).

In conclusion of the analysis of the thermal field, we postulate that agreement between experiments and simulations is still not satisfactory. This disagreement is most probably a consequence of a combination of the used measuring techniques and still some uncounted experimental heat losses since the numerical simulation profiles exhibit typical behavior in a close agreement with similar studies in the literature.

5. Conclusions and outlook

A new experimental campaign was conducted at VKI on a forced planar jet with heated co-flow at two values of Prandtl number, Pr = 0.71 (air) and 0.2 (He-Xe gas mixture). The PIV and thermocouple measurement data were used to validate the RANS simulations, which included a series of approaches ranging from a standard two-equation $k - \varepsilon$ to the state-of-art low-Reynolds elliptic-relaxation based $\zeta - f$ model. For temperature field predictions, a range of turbulent heat flux models was applied, ranging from the standard constant turbulent Prandtl number approach to a more elaborate $k_\theta - \varepsilon_\theta$ models. Overall good agreement between the experiments and simulations in predicting the cross-wise profiles of the mean velocity, turbulent kinetic energy

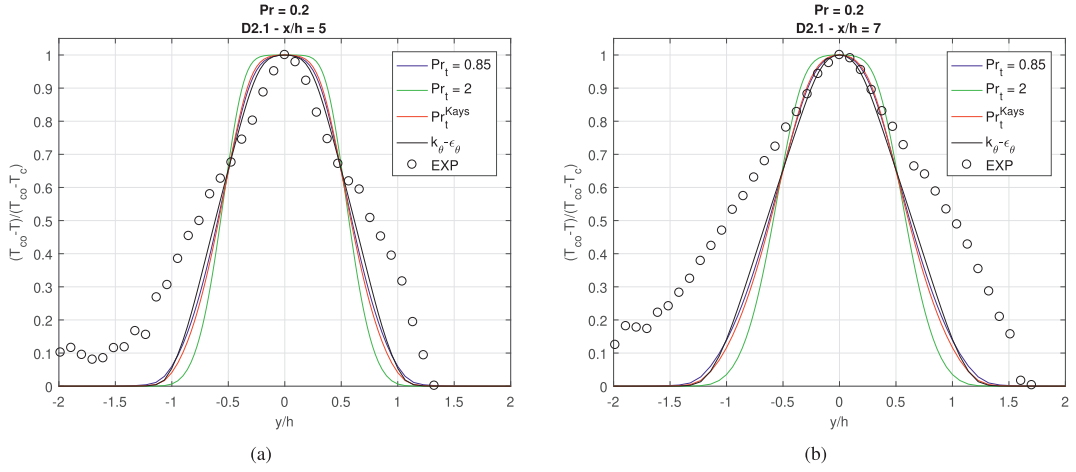

Fig. 12. Profiles of normalized temperature at Pr = 0.2 with different THT models from domain D2.1 at different locations (a, b).

and turbulent shear stress at different locations. The quality of agreement was improved when typical asymmetrical inlet conditions were imposed at the co-flow inlet planes. In contrast to the velocity field, the temperature profiles showed a good agreement in the central part of the domain (i.e. within the central jet region), whereas significant deviations were observed in the co-flow and connecting regions. A rather small differences between different turbulent heat flux models, which ranged from a standard constant turbulent Prandtl number to a more comprehensive model based on the solving of additional equations for the temperature variance and its dissipation rate ($k_\theta - \varepsilon_\theta$), indicated an overall dominance of the strong convective forced convection and passive behavior of the temperature. The more advanced models of the turbulent heat flux considered here will have a significantly more important role for mixed and especially natural convection situations involving low Prandtl fluids.

CRediT authorship contribution statement

E. Cascioli: Methodology, Software, Validation, Formal analysis, Data curation, Writing - original draft, Writing - review & editing, Visualization. **S. Buckingham:** Validation, Formal analysis, Investigation, Writing - original draft, Visualization. **S. Keijers:** Supervision, Writing - original draft. **K. Van Tichelen:** Resources, Writing - original draft, Supervision, Project administration, Funding acquisition. **Sasa Kenjeres:** Methodology, Formal analysis, Resources, Data curation, Writing - original draft, Writing - review & editing, Supervision, Project administration, Funding acquisition.

Declaration of Competing Interest

The authors declare that they have no known competing financial interests or personal relationships that could have appeared to influence the work reported in this paper.

Acknowledgment

This work was supported by European Commission's H2020-EURATOM program under Grants 654935 (SESAME) and 662186 (MYRTE).

References

Abe, K., Kondoh, T., Nagano, Y., 1995. A new turbulence model for predicting fluid flow and heat transfer in separating and reattaching flows – II. Thermal calculations. Int. J. Heat Mass Transfer 38 (8), 1467–1481.

Back, H.L., Cuffel, R.F., Massier, R.F., 1970. Laminarization of a turbulent boundary layer in nozzle flow – Boundary layer and heat transfer measurements with wall cooling. J. Heat Transfer 92 (3), 333–344.

Bogey, C., Bailly, C., 2009. Turbulence and energy budget in a self-preserving round jet: direct evaluation using large eddy simulation. J. Fluid Mech. 627, 129–160.

Buckingham S., 2018. Experimental results on BFS and jet flow test case. MYRTE D3. 14-v3.

Chua, L.P., Antonia, R.A., 1990. Turbulent Prandtl number in a circular jet. Int. J. Heat Mass Transfer 33 (2), 331–339.

Da Via, R., Manservisi, S., Menghini, F., 2016. A (k-Ω-k_θ-Ω_θ) four parameter logarithmic turbulence model for liquid metals. Int. J. Heat Mass Transfer 101, 1030–1041.

Di Venuta, I., Boghi, A., Angelino, M., Gori, F., 2018. Passive scalar diffusion in three-dimensional turbulent rectangular free jets with numerical evaluation of turbulent Prandtl/Schmidt number. Int. Commun. Heat Mass Transfer 95, 106–115.

Durbin, P.A., 1995. Separated flow computations with the k-$\varepsilon - \overline{v^2}$ model. AIAA J. 33, 659–664.

Errico, O., Stalio, E., 2015. Direct numerical simulation of low Prandtl number turbulent convection above a wavy channel. Nucl. Eng. Design 290, 87–98.

Fernandez R., De Bruyn D., Baeten P., Ait Adberrahim H., 2017. The evolution of the primary system design of the MYRRHA facility. IAEA-CN-245-258.

Franco-Medrano, F., Fukumoto, Y., Velte, C., Hodzic, A., 2017. Mass entrainment rate of an ideal momentum turbulent round jet. J. Phys. Soc. Jpn. 86, 034401–034427.

Fregni, A., Angeli, D., Cimarelli, A., Stalio, E., 2019. Direct numerical simulation of a buoyant triple jet at low-prandtl number. Int. J. Heat Mass Transf. 143.

Grotzbach, G., 2013. Challenges in low-Prandtl number heat transfer simulation and modelling. Nucl. Eng. Des. 264, 41–55.

Hanjalić, K., Kenjereš, S., Durst, F., 1996. Natural convection in partitioned two-dimensional enclosures at higher Rayleigh numbers. Int. J. Heat Mass Transf. 39 (7), 1407–1427.

Hanjalić, K., Popovac, M., Hadžiabdić, M., 2004. A robust near-wall elliptic-relaxation eddy-viscosity turbulence model for CFD. Int. J. Heat Fluid Flow 25, 1047–1051.

Jones, P.W., Launder, B.E., 1972. The prediction of laminarization with a two equation model of turbulence. Int. J. Heat Mass Transf. 15, 301–314.

Kader, B.A., 1981. Temperature and concentration profiles in fully turbulent boundary-layers. Int. J. Heat Mass Transf. 24 (9), 1541–1544.

Kays, W.M., 1994. Turbulent Prandtl number – Where are we? J. Heat Transfer 116, 284–295.

Kenjereš, S., Hanjalić, K., 2000. Convective rolls and heat transfer in finite-length Rayleigh-Benard convection: a two-dimensional numerical study. Phys. Rev. E 62 (6), 1–12.

Kenjereš, S., Gunarjo, S.B., Hanjalić, K., 2005. Contribution to elliptic relaxation modelling of turbulent natural and mixed convection. Int. J. Heat Fluid Flow 26, 569–589.

Kimura, N., Miyakoshi, H., Kamide, H., 2007. Experimental investigation on transfer characteristics of temperature fluctuation from liquid sodium to wall in parallel triple-jet. Int. J. Heat Mass Transf. 50, 2024–2036.

Knebel, U., Krebs, L., Muller, U., Axcell, B.P., 1998. Experimental investigation of a confined heated sodium jet in a co-flow. J. Fluid Mech. 368, 51–79.

Launder, B.E., Spalding, D.B., 1973. The numerical computation of turbulent flows. Computed Methods Appl. Mech. Eng. 3, 269–289.

Le Ribault, C., Sarkar, S., Stanley, A., 1999. Large eddy simulation of a plane jet. Phys. Fluids 11 (10), 3069–3083.

Lien, F.S., Kalitzin, G., 2001. Computations of transonic flow with the $v^2 - f$ turbulence model. Int. J. Heat Fluid Flow 22, 53–61.

Manservisi, S., Menghini, F., 2014. A CFD four parameter heat transfer turbulence model for engineering applications in heavy liquid metals. Int. J. Heat Mass Transf. 69, 312–326.

Manservisi, S., Menghini, F., 2015. CFD simulations in heavy liquid metal flows for square lattice bare rod bundle geometries with a four parameter heat transfer turbulence model. Nucl. Eng. Des. 295, 251–260.

Moser, R.D., Kim, J., Mansour, N.N., 1999. Direct numerical simulation of turbulent channel flow up to $Re_\tau = 590$. Phys. Fluids 11 (4), 943–945.

Otić I., Class A., 2007. Numerical investigation of a heated sodium jet in a co-flow. FEDSM2007-37566.

Pope, S.B., 2000. Turbulent Flows. Cambridge University - Cambridge Univ. Press.

Roelofs, F., Shams, A., Otić, I., Bottcher, M., Duponcheel, M., Bartosiewicz, Y., Lakehal, D., Baglietto, E., Lardeau, S., Cheng, X., 2015. Status and perspective of turbulence heat transfer modelling for the industrial application of liquid metal flows. Nucl. Eng. Des. 290, 99–106.

Tenchine, D., Vandroux, S., Barthel, V., Cioni, O., 2013. Experimental and numerical studies on mixing jets for sodium cooled fast reactors. Nucl. Eng. Des. 263, 263–272.

Van Tichelen, K., Mirelli, F., Greco, M., Viviani, G., 2015. E-SCAPE: a scale facility for liquid-metal, pool-type reactor thermal hydraulic investigations. Nucl. Eng. Des. 290, 65–77.

Versteeg, H.K., Malalasekera, W., 1995. An introduction to computational fluid dynamics – The finite volume method Longman Scientific & Technical.